Journal of Applied Mathematics and Physics, 2024, 12, 3842-3859
https://www.scirp.org/journal/jamp
ISSN Online: 2327-4379
ISSN Print: 2327-4352

Influence of Scanning Patterns on Mechanical Behavior and Distortion in Laser Directed Energy Deposition

Qi Wang, Bingjie Xiao, Shaopeng Zheng*

College of Construction Engineering, Jilin University, Changchun, China
Email: wq1113455063@163.com, x19832198681@163.com, *zhengsp0428@jlu.edu.cn

How to cite this paper: Wang, Q., Xiao, B.J. and Zheng S.P. (2024) Influence of Scanning Patterns on Mechanical Behavior and Distortion in Laser Directed Energy Deposition. *Journal of Applied Mathematics and Physics*, **12**, 3842-3859.
https://doi.org/10.4236/jamp.2024.1211231

Received: October 22, 2024
Accepted: November 22, 2024
Published: November 25, 2024

Abstract

Laser Directed Energy Deposition (LDED) marks a critical advance in intelligent manufacturing, enabling efficient near-net shape production of metal parts. This method is especially beneficial for aerospace and defense applications that require high precision. However, issues such as deformation and heat accumulation during production still affect the quality of the final products, necessitating further optimization of process parameters. This paper studies the effects of three deposition strategies on 316L stainless steel parts using LDED. The three strategies based on unidirectional scanning (US), zigzag scanning (ZS), and square spiral scanning (SS) are investigated by solid samples and samples with a central hole. The surface smoothness, defects, and mechanical properties of 316L samples manufactured with the above strategies are discussed by means of surface topography tests and metallographic characterization. Experimental results indicate that the zigzag scanning strategy yielded better results for solid components, and the square spiral scanning strategy is suitable for samples with a central hole.

Keywords

Directed Energy Deposition, Deposition Strategy, 316L Stainless Steel, Microstructure, Microhardness, Surface Smoothness

1. Introduction

Laser Directed Energy Deposition (LDED) is an additive manufacturing technique that utilizes a high-power laser to melt metal powder particles emitted from the nozzle onto a substrate. This process allows for precise control over material addition, making it suitable for applications such as repairing components, creating

complex geometries, enhancing material properties, and significantly extending the lifespan of components while reducing production costs [1]. Moreover, it supports innovations in various industries, including aerospace, automotive, and biomedical, by providing a flexible and efficient approach to material processing [2]-[5].

Inter-layer path planning is a critical aspect of the LDED process that significantly influences the quality and efficiency of the additive manufacturing process [6]-[8]. Effective path planning ensures optimal material deposition, minimizing defects such as porosity and ensuring uniform layer adhesion. By strategically determining the sequence and orientation of the deposition paths, it is possible to enhance thermal management, reduce residual stresses, and improve surface finish. In the LDED process, path planning methods are generally categorized into the following forms: geometric-based path planning, optimization-based path planning, and simulation-based path planning.

For geometric-based path planning strategies, some related studies provide manufacturing paths based on the geometric shape and structural features of parts to achieve efficient coverage and precise control over the parts. Common methods include straight-line deposition, contour following, and so on. The rapid computation of zigzag trajectories using straight lines and circular arcs was proposed by Rajan *et al.* [9] in the early. Jin *et al.* [10] put forth an adaptive strategy that enhances RP/M process planning for complex models. This strategy employs non-uniform rational B-spline-based curves for accurate boundary representation and a mixed tool-path algorithm for efficient fabrication. Syed *et al.* [11] examined how oscillation and parallel pass deposition strategies affect the tensile and high cycle fatigue properties of as-built wire + arc additive manufactured Ti-6Al-4V alloy. Bi *et al.* [12] introduced a framework for generating continuous toolpaths in LFAM for solid and partial infills. It employed outward contour and double offset strategies for primary paths and extended zigzag lines for remaining areas, linking layers via a depth-first search. Veiga *et al.* [13] evaluated the use of plasma arc welding (PAW) for additive manufacturing SS316L-Si X-cross intersections, focusing on geometry and productivity. They presented two production strategies: energy control for L-shaped walls and variable amplitude waveforms for continuous X-cross production. Tarchoun *et al.* [14] [15] conducted experimental studies on the laser surface hardening of AISI 4340 steel using various laser scanning methods. They found that the maximum hardening width is achieved with the sine mode. Additionally, detailed modeling and simulation work was performed based on three-dimensional finite element thermal analysis, along with practical research structured according to the Taguchi method. The results indicate that the proposed numerical models can provide robust and accurate estimates of surface hardening characteristics under varying heating parameters and scanning modes. Demin *et al.* [16] investigated a new laser plasma deposition method and discovered that the deposition rate and coating structure are influenced by the HMDS flow rate and the process parameters of the plasma-generating gas (either Ar or a mixture of Ar and He).

The optimization-based path planning approaches utilized algorithms such as genetic and ant colony optimization to identify optimal paths based on part geometry, material characteristics and manufacturing specifications, thereby enhancing efficiency and quality. A sequential path-planning method for wire and arc additive manufacturing (WAAM), based on the water-pouring rule, was proposed by Wang *et al.* [17] as a means of densifying internal structures and accelerating response times. It relocated intersections to the outer contour, thereby ensuring a uniform and compact inner area. Singh *et al.* [18] employed a Travelling Salesman Problem (TSP)-based algorithm for the efficient and accurate generation of toolpaths in the area filling, thereby reducing the necessity for retractions and turns. The layer was digitized into a grid of points, which were then filled in sequence by the deposition head, thus ensuring the absence of voids. Petrik *et al.* [19] developed a path planning framework that made use of reinforcement learning as well as automated prepositional and sequential least squares programming optimization methods to deal with thin-walled structures in wire arc additive manufacturing.

For the simulation-based path planning, it employed numerical models to predict thermal stresses and deformations in additive manufacturing, guiding optimized toolpaths through multiphysics simulations for enhanced accuracy and efficiency. Foroozmehr *et al.* [20] employed ANSYS finite element software to simulate temperature and stress fields in laser powder deposition, assessing how deposition patterns influence final stress distribution. Sun *et al.* [21] developed a novel S-pattern for metal additive manufacturing and analyzed its effects on the temperature and stress fields of a cuboid structure compared to five other patterns using the finite element method. Ren *et al.* [22] presented a framework for simulating and evaluating laser scanning paths with finite element models for three-dimensional thermal history analysis. This allowed them to determine the optimal scanning pattern with minimal distortion. Zhou *et al.* [23] utilized a genetic algorithm-based method for planning continuous tool-paths with optimal thermo-mechanical properties. Based on investigations for material characteristics of turning-style toolpath strategies, Feldhausen *et al.* [24] leverage existing CAM technology for turning, where the component rotates around a stationary cutting tool, to generate toolpath trajectories for DED with varying wall thicknesses and controlled deposition angles.

In this paper, experiments were conducted on six 316L stainless steel samples to compare the surface flatness, microstructure, and defects of samples fabricated using three common deposition strategies: unidirectional scanning (US), zigzag scanning (ZS), and square spiral scanning (SS). The investigation focused on surface flatness and included scanning electron microscopy analyses of 316L components with holes produced by these methods, highlighting the impact of different deposition strategies on the quality of the formed parts.

2. Experimental Materials and Methods

In this study, a total of six experimental samples divided into two groups were first

manufactured using a 3D printer. Following the cutting, grinding, and polishing of the samples, a series of tests were conducted. These included surface finish analysis, X-ray diffraction (XRD) measurements, determination of density, porosity testing via scanning electron microscopy (SEM), and microhardness testing. Figure 1 illustrates the workflow of the entire experimental process described in the paper, while Figure 2 presents the equipment diagram for the whole experiment.

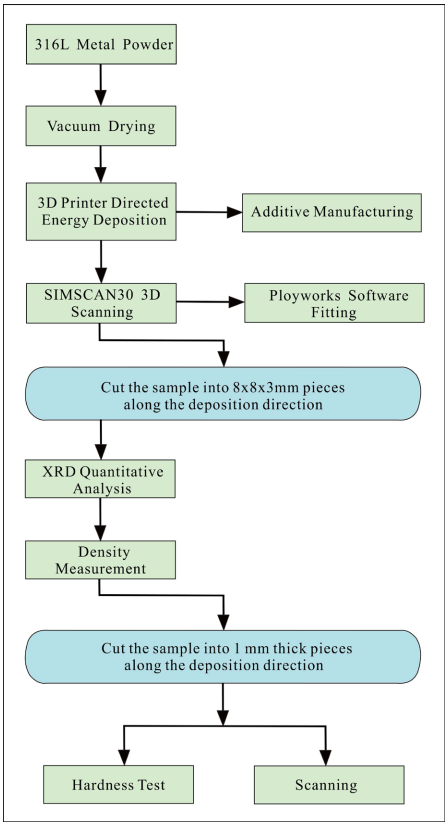

Figure 1. Experimental detailed flow chart.

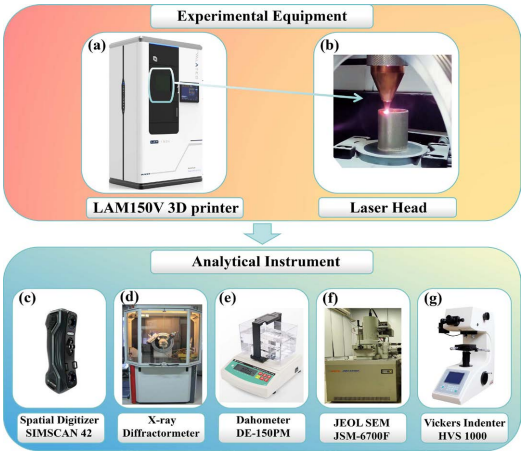

Figure 2. Experimental equipment and analytical instrument for the DED process: (a) DED machine tools; (b) laser head; (c) spatial digitizer; (d) XRD; (e) densitometer; (f) SEM; (g) Vickers indenter.

The 3D printing equipment used in this study is the LAM150V five-axis inert gas-protected 3D printer. The laser spot diameter ranges from 0.5 mm to 1.5 mm, and argon is used as the shielding gas to maintain low oxygen content throughout the manufacturing process. For the directed energy deposition experiment, a 316L stainless steel substrate measuring 150 mm × 150 mm × 15 mm was selected. Prior to cladding, the substrate's surface was treated with sandpaper to remove oil and oxide layers and then wiped with alcohol to ensure a good metallurgical bond between the printing layer and the substrate. The 316L metal powder used for the experiment had a particle size range of 53 μm to 105 μm, with an average particle size of approximately 75 μm. **Figure 3(a)** shows the morphology of the 316L powder used in the DED research, while **Figure 3(b)** presents the size distribution curve. To ensure good flow performance of the metal powder during laser processing, the powder was dried at 120˚C for two hours in a vacuum oven before the experiment. **Table 1** lists the elemental composition of the metal powders.

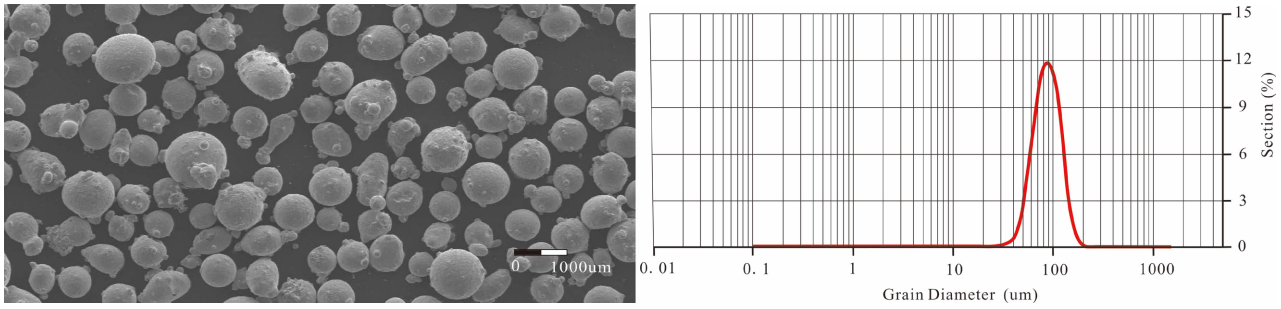

(a) (b)

Figure 3. (a) electron microscopic image of 316L powder particles; (b) powder particle size distribution map.

Table 1. Chemical composition of 316L powder.

Element	Fe	Cr	Ni	Mo	Si	Mn	C	S	O	P
Powder (wt%)	Bal	17.30	10.83	2.42	0.39	0.49	0.009	0.005	0.039	0.025

Prior to the commencement of the experiment, printing tests were conducted on single-layer, six-channel samples utilizing twelve distinct parameter combinations. These combinations included two different laser powers (500 W and 600 W), two different powder feed rates (4 g/min and 6 g/min), and three different overlap rates (0%, 25%, and 50%), as shown in **Figure 4**. Based on surface smoothness, cladding quality, and printing efficiency, it was observed that the optimal overall printing performance was achieved with an overlap rate of 25%, a laser power of 500 W, and a powder feed rate of 4 g/min. Therefore, the specific process parameters for the subsequent experiments are as follows: laser power P = 500 W, scanning speed V = 4 mm/s, powder feed rate v = 4 g/min, the distance from the contact tip to the workpiece is maintained at 10 mm, and the substrate is not preheated.

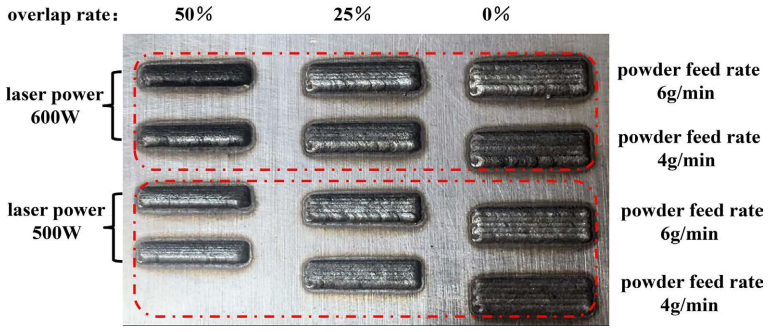

Figure 4. Single-layer six-track printing samples at different bonding rates, laser power and powder delivery rates.

Haolin *et al.* [25] reviewed various scanning strategies in the laser melting process, including zigzag scanning, unidirectional scanning, and continuous scanning. They found that interlayer rotation of the printing direction—rotating the heat flow during the printing process—promotes a uniform distribution of material. However, their study only considered the printing of solid square samples. In this paper, we also employed interlayer rotating printing and analyzed three strategies for printing hollow square samples to determine which strategy is most suitable for this specific case. Three principle deposition strategies, unidirectional, zigzag and square spiral scanning, were used in the trials for both hollow square samples and solid square samples. The unidirectional scanning means that the deposition direction of adjacent welds is the same and parallel to the y-axis direction, with the scanning path of adjacent deposition layers rotated by 90˚. The zigzag scanning involves continuous deposition without extinguishing the arc, with the scanning path of adjacent deposition layers also rotated by 90˚. This rotation of the heat flow direction during printing is more conducive to achieving a uniform temperature distribution [26]. The square spiral scanning starts at the center and deposits in a clockwise spiral, with each layer repeating the deposition method of the first layer (the green dot represents the deposition starting point, and the purple dot represents the deposition endpoint). The geometry for the solid square samples is depicted in **Figure 5(a)**. **Figure 5(b)** and **Figure 5(c)** show the three-layer path planning of the solid square samples for the three deposition strategies, respectively. A cube with a side length of 31 mm and a height of 3 mm was printed in three layers, as listed in **Figure 6(a)**. **Figure 6(b)** and **Figure 6(c)** show the path planning of the second type samples for the three deposition strategies, where a cube with a side length of 28 mm and a height of 3 mm was printed in three layers with a central hole of 8 mm side length and 3 mm height.

The samples obtained in the experiment were scanned using the SIMSCAN30 3D scanner, which has an accuracy of 0.0175 mm. The scanned images were imported into PolyWorks software for fitting and comparison. The surface flatness of the experimental samples, obtained under different scanning strategies, was evaluated by fitting from the lowest point of the plane.

Quantitative phase analysis was conducted using an X-ray diffractometer (XRD). Prior to the XRD study, six sample blocks were cut into 8 mm × 8 mm × 3 mm

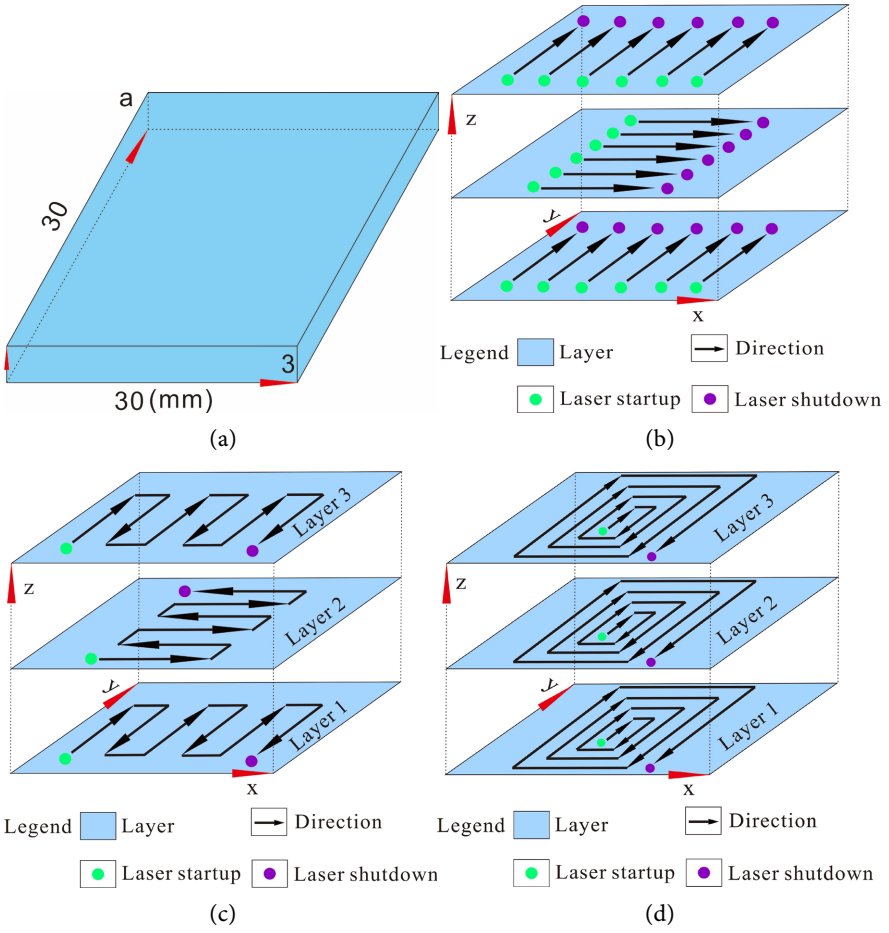

Figure 5. Printing strategy schematic: (a) geometry for the solid square sample; (b) unidirectional scanning for the solid square sample (SUS); (c) zigzag scanning for the solid square sample (SZS); (d) spiral scanning for the solid square sample (SSS).

blocks along the deposition direction using wire electrical discharge machining (EDM) to facilitate subsequent material characterization. The samples were ultrasonically cleaned with ethanol, ground, and polished using sandpaper with grit sizes ranging from 240 to 1000. XRD was then used to perform qualitative analysis on the 316L powder and the DED processed samples. The tube voltage was set to 40 KV, and the current to 30 mA, with a starting angle of 20˚ and an ending angle of 90˚. For further polishing, sandpaper with grit sizes ranging from 240 to 5000 was used. The density of the six DED samples was measured using the Archimedes method [27]. A plastic electronic density meter is essential for this procedure. The specific steps involve calibrating the meter using a standard weight, placing the sample on the measuring table, and then waiting for the test results to be displayed and recorded. The final data should be obtained by averaging multiple measurements to ensure accuracy. Each sample's density was measured three times, and the average value was taken. Additionally, these six samples were longitudinally cut into approximately one-millimeter-thick sections. The previously specified grinding and polishing procedures were then applied to these portions. The samples

were then scanned using a JSM-6700F scanning electron microscope.

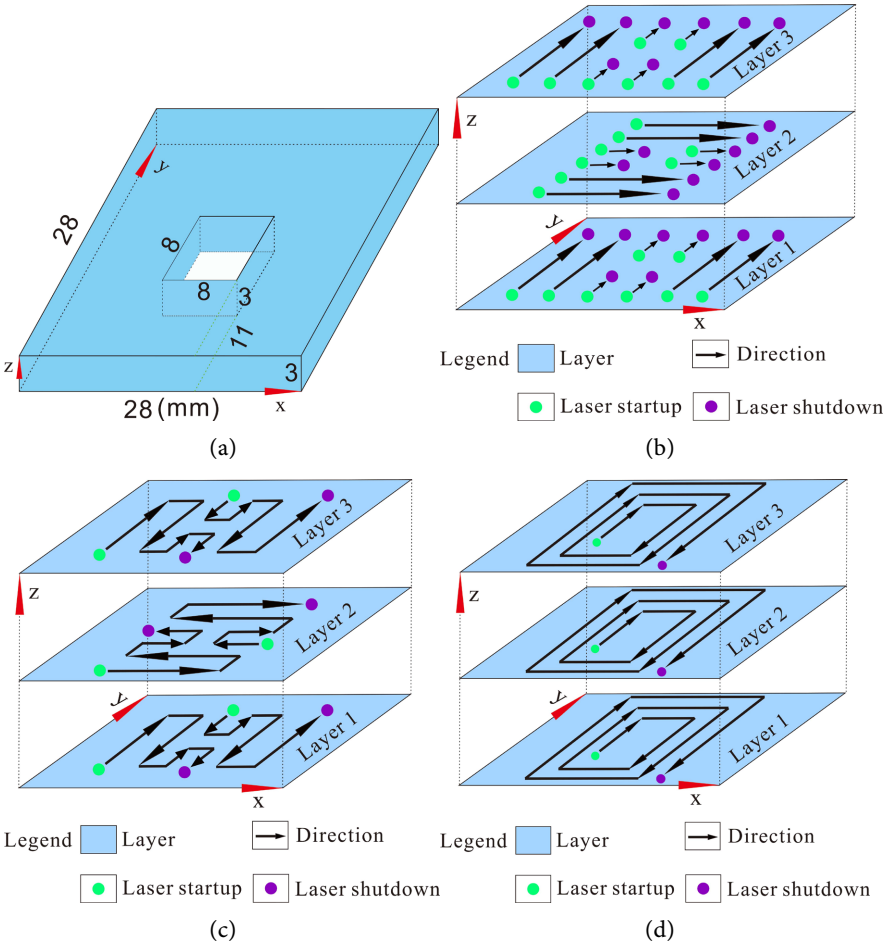

Figure 6. Printing strategy schematic: (a) geometry for the hollow square sample; (b) unidirectional scanning for the hollow square sample (HUS); (c) zigzag scanning for the hollow square sample (HZS; (d) spiral scanning for the hollow square sample (HSS).

The Vickers microhardness tester (FM300e, Future-Tech Corp., Kawasaki, Japan) was used to measure material density via the indentation method. The procedure involved placing the sample on the test bench and ensuring that its surface was perpendicular to the indenter. The eyepiece was adjusted to clearly observe the sample's surface. A load of 100 N was applied, and the test force was initiated, with an average indentation retention time of 10 seconds. The experiment involved measuring the microhardness of six specimens. Each sample was measured at 24 points along the transverse and longitudinal directions, with an interval distance of 0.1 mm. The load was set to 100 N, and the average indentation dwell time was 10 seconds.

As shown in **Figure 7(a)**, the test positions were divided into two parts: the transverse plane and the longitudinal plane. **Figure 7(b)** and **Figure 7(c)** depict the points obtained under the microscope for the transverse and longitudinal directions, respectively.

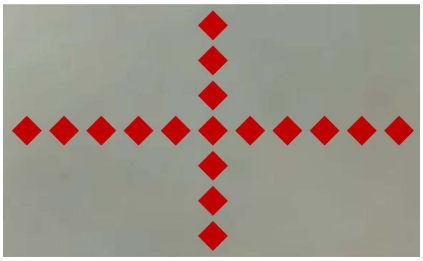

(a)

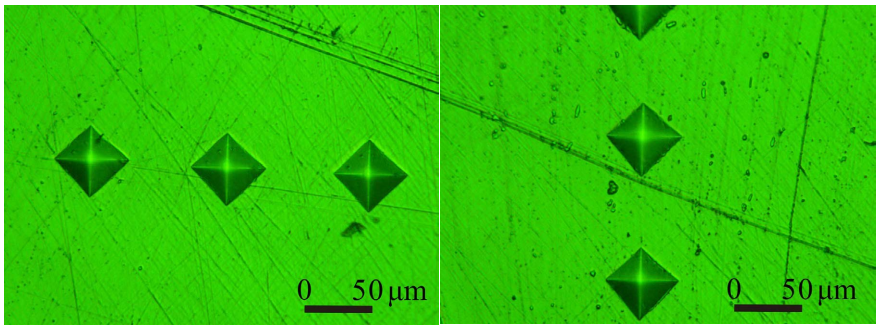

(b) (c)

Figure 7. (a) sample hardness test point diagram; (b) sample transverse microhardness test site diagram; (c) sample vertical microhardness test site diagram.

3. Experimental Results and Discussion

3.1. Geometry of the Samples Obtained for Each Printing Strategies

Figure 8 and **Figure 9** show the solid square parts, the hollow square parts, and the corresponding 3D scan fitting for the three deposition strategies. The colors closer to red indicate greater deformation. For the solid square scan strategy, the unidirectional scanning (SUS) strategy exhibits relatively less deformation, followed by the zigzag scanning (SZS) strategy, and the square spiral scanning (SSS) strategy shows relatively larger deformation. The SZS processed part shows more pronounced deformation at the edges, while the SUS processed part exhibits more uniform deformation. The SSS processed part shows uneven deformation, with four distinct edges dividing the printed part into four triangular regions, where the color gradually weakens clockwise. For the hollow square scan strategy, the unidirectional scanning (HUS) strategy exhibits relatively less deformation, followed by the square spiral scanning (HSS) strategy, and lastly, the zigzag scanning (HZS) strategy shows relatively larger deformation. The HZS processed part shows less surface deformation overall but exhibits significant local defects and holes, with four distinct edges visible. Overall, it is evident that the hollow square samples show significantly greater surface deformation compared to solid ones.

By observing the printing process of the samples under the three deposition strategies, minimizing short-edge printing is essential to achieve relatively low deformation. From the 3D scan entity fitting graph, it's evident that the SZS method induces significant edge deformation. This is due to continuous laser printing in zigzag scanning causes small inflection points and subsequent short-edge printing

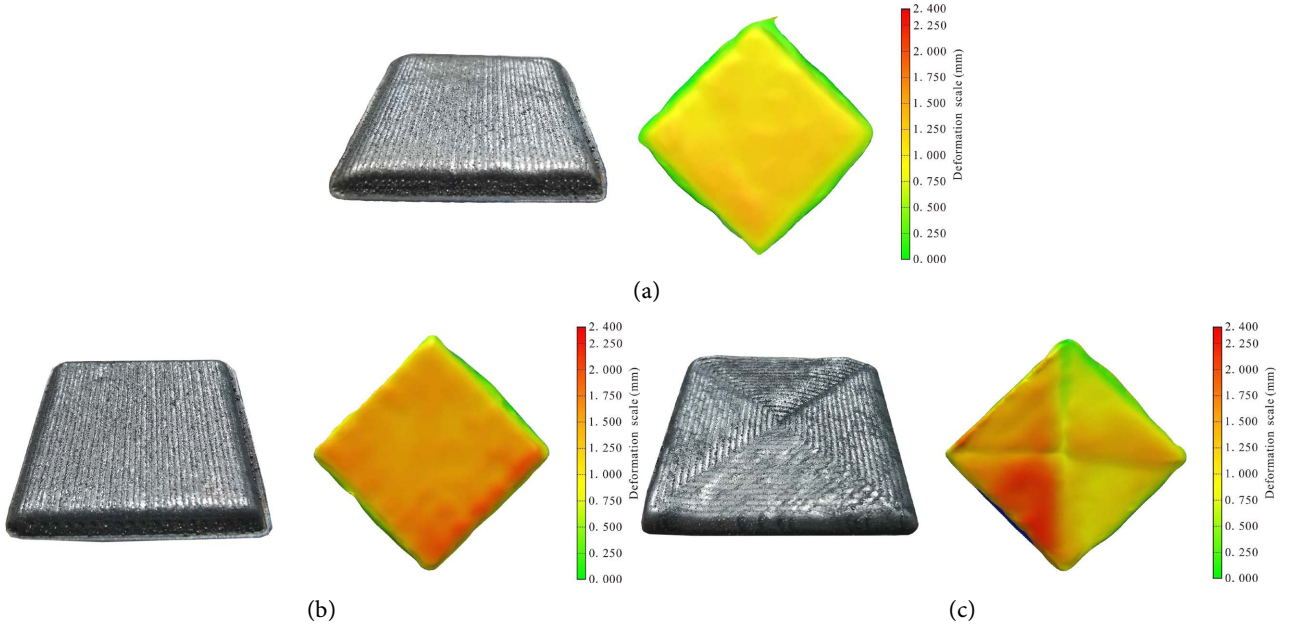

Figure 8. Solid squares parts under three scanning strategies and 3D fitting graph under three scanning strategies: (a) SUS; (b) SZS; (c) SSS.

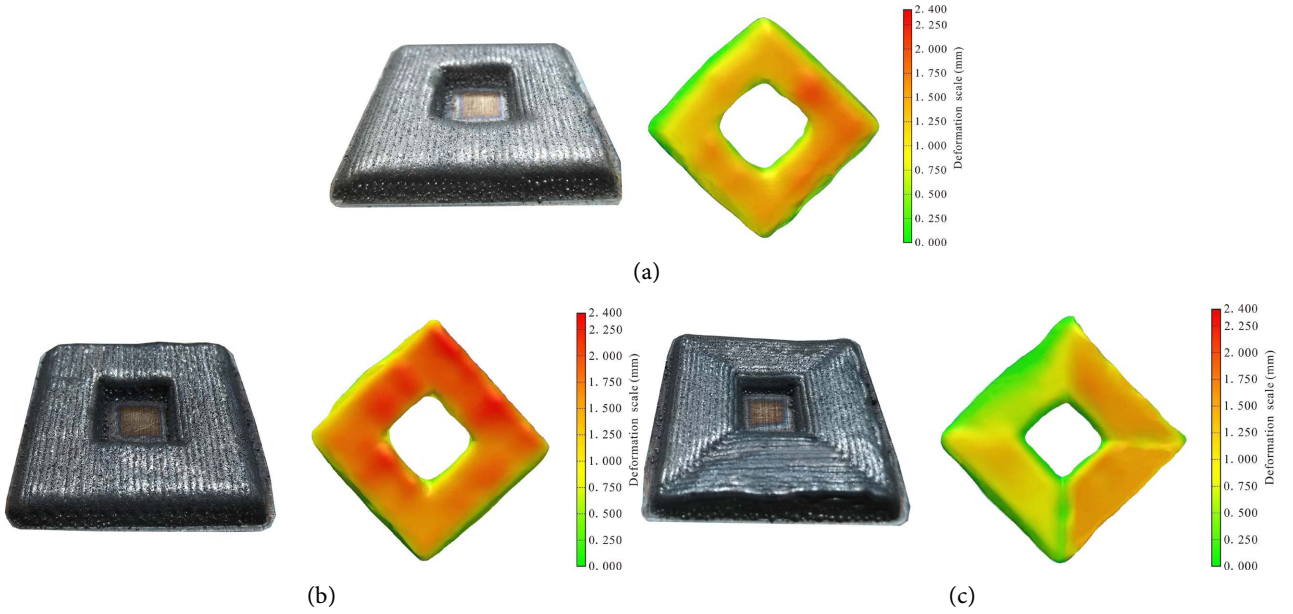

Figure 9. Hollow squares parts under three scanning strategies 3D fitting graph under three scanning strategies: (a) HUS; (b) SZS; (c) HSS.

at the endpoints. Moreover, when comparing the hollow square printing strategy to the solid square printing strategy, greater deformation occurs due to increased short-edge printing. Excessive short-edge printing leads to higher heat accumulation, resulting in more pronounced surface deformation. To ensure more uniform deformation, a consistent overlap rate is crucial. The surface deformation with the SUS sample remains smaller and more uniform because the overlap rate remains constant, and short-edge printing is avoided. Conversely, square spiral scanning

exhibit distinct four-edge patterns. The uneven melt pool, caused by inconsistent scanning speeds, contributes to this phenomenon. As the laser beam direction changes from horizontal to vertical, there is an initial decrease and subsequent increase in acceleration, resulting in slower speeds at corners and sharp temperature rises. This secondary sintering phenomenon leads to localized collapse formation. Additionally, larger distances at turn-back inflection points, as shown in Figure 10, contribute to lower bonding rates. With increased heat accumulation from stacking layers, deformation gradually intensifies, particularly noticeable at lower bonding rates. Furthermore, the printing strategy shows progressively smaller areas of deformation in the four triangle regions. This phenomenon can be attributed to the early increase and subsequent elongation of short-edge printing, which results in a greater accumulation and deformation of heat. Secondly, the laser printing process facilitates the preheating of subsequent layers, thereby promoting more consistent printing.

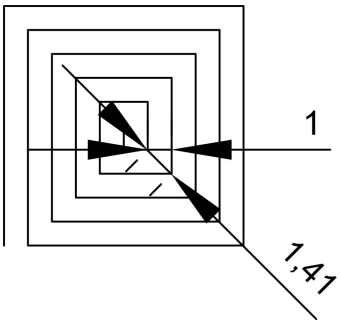

Figure 10. Square spiral scanning plan sketch.

3.2. XRD Diffraction Experiment

Figure 11 depicts the XRD patterns of the samples prepared using 316L powder with three scanning strategies: SUS, SZS, SSS, and also with HUS, HZS, and HSS, all conducted under a laser power of 500 W and a scanning speed of 4 mm/s. The XRD analysis revealed no significant phase transitions during the DED process or post-processing, with diffraction peak positions remaining consistent. Similar findings were reported by Shin *et al.*, although notable differences were observed in the intensity of the diffraction peaks [28].

The difference in diffraction peak intensity is primarily due to changes in crystal texture, indicating variations in crystal orientation distribution under different printing strategies. As shown in Figure 11(a) and Figure 11(b), the SZS scanning strategy leads to an increase in the principal diffraction peak intensity for both solid printing and printing with intermediate perforations. This is because, under this strategy, long-edge printing is more prevalent, causing the microstructure of the sample to preferentially orient, resulting in elongated columnar grains and higher principal diffraction peaks. In contrast, during the early stages of laser processing with the SSS scanning strategy, there are more spiral short-edge prints. Consequently, the microstructure of the specimens tends to be randomly oriented,

exhibiting non-directional growth. This results in a higher proportion of irregular coarse equiaxed grains and relatively weaker main diffraction peaks [29]. Due to the holes in the middle of the scanning strategy with HSS, there are fewer short edges in the early stages of laser processing. Therefore, the main diffraction peak diagram of test pieces prepared with the HSS scanning strategy is slightly higher than that of the SSS scanning strategy. Compared to the two solid printing strategies, SZS and SUS, the two printing strategies with holes, HZS and HUS, involve more short-edge printing. As a result, the main diffraction peak diagram of the printed test pieces with holes is slightly lower than that of the solid printed test pieces under these two methods.

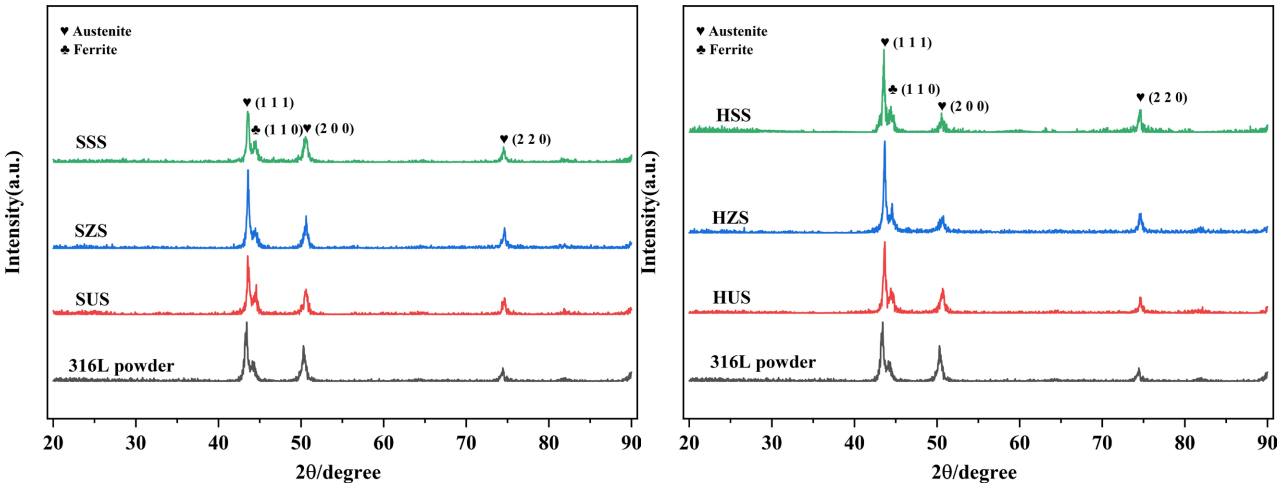

Figure 11. (a) the XRD patterns of 316L powder, SUS, SZS, and SSS; (b) the XRD patterns of 316L powder, HUS, HZS, and HSS.

3.3. Scanning Electron Microscopy

Figure 12 shows the profile morphology of 316L samples prepared by the DED process under the three scanning strategies. It can be observed from the figure that relatively obvious defects of unfused pores are present in the profile under electron microscope scanning. These defects arise due to insufficient energy density, leading to incomplete fusion of powder particles. In such pores, the shape is irregular, and powder particles are observed inside [30]. **Figure 12(a)**, **Figure 12(c)**, and **Figure 12(e)** show the profile electron microscopy of the printed solid square samples under the three printing strategies. It can be seen that more and larger pore defects appear under the SUS scanning strategy, while the samples printed under the SSS scanning strategy show relatively smaller pore defects. **Figure 12(b)**, **Figure 12(d)**, and **Figure 12(f)** show the electron microscope images of the hollow square sample using the three printing strategies. For the HUS scanning strategy, there are still more and larger pore defects, whereas relatively smaller pore defects are found in samples printed under the HZS scanning strategy. The presence of more and larger pore defects under SUS and HUS scanning strategies is due to the instability of laser power during the process, which is

caused by higher laser frequency switching under unidirectional scanning strategies. This instability leads to poor interlayer bonding and the formation of large local unfused pores. For the same scanning strategy, the hollow square samples (HUS and HZS) exhibit fewer and smaller pores compared to SUS and SZS samples, respectively. This is because the middle holes result in more short-edge printing, causing greater heat accumulation and more thorough melting of powder particles. Similarly, the HSS sample, with its relatively more short-edge spiral printing compared to the SSS sample, results in more complete powder melting and closer interlayer bonding.

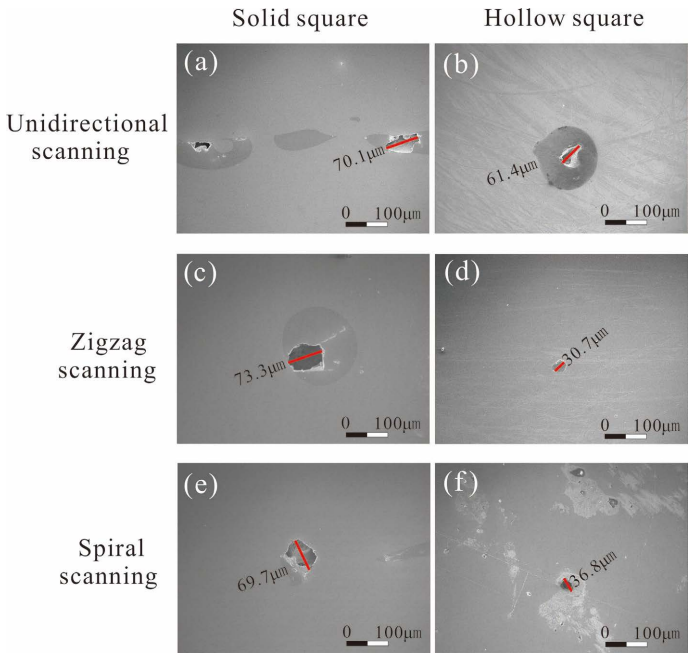

Figure 12. Electron microscope image: (a) SUS; (b) HUS; (c) SZS; (d) HZS; (e) SSS; (f) HSS.

3.4. Density Test and Hardness Test

The measured densities are summarized in **Table 2**. It can be seen that the density of printed solid square parts and hollow square parts under different scanning strategies is not much different.

Hardness testing is primarily used to evaluate the mechanical properties of materials. **Figure 13(a)**, **Figure 13(b)** show the hardness curves of solid square parts and hollow square parts of the sample along the transverse measurement, respectively. The small bar charts in the figures represent the average hardness values under each strategy. As shown in **Figure 13(a)**, the average hardness of the SZS sample is 213.6 HV, the one for the SSS sample is 212.2 HV, and the lowest average hardness is 197.9 HV for the SUS scanning strategy. In **Figure 13(b)**, the average hardness of the hollow square test pieces in the middle reached 212.3 HV under the HUS scanning strategy, while the lowest average hardness was observed under the HSS scanning strategy. By comparing **Figure 12(a)** and **Figure 12(b)**, it is

evident that the microhardness of the hollow square samples using the HUS and HZS strategies is reduced compared to those printed with the SUS and SZS strategies. This reduction in hardness is due to an increase in the number of short-edge printing passes for samples with holes, leading to greater heat accumulation and a smaller temperature gradient. This results in a slower cooling rate, thereby reducing hardness [31]. However, the microhardness of the perforated test pieces printed by the HSS strategy does not decrease compared to the solid test pieces printed by the SSS strategy. This is because the presence of intermediate holes in the HSS scanning strategy significantly reduces short-edge printing, leading to less heat accumulation and, consequently higher hardness.

Table 2. Measured densities of solid parts and holes printed under three scanning strategies.

Sample piece	Density g/cm³		Density g/cm³	
SUS	7.8563	7.8506	7.8959	7.8676
SZS	7.8445	7.8501	7.8445	7.8464
SSS	7.9064	7.8904	7.8972	7.8980
HUS	7.8900	7.8291	7.8342	7.8511
HZS	7.8526	7.8419	7.8472	7.8472
HSS	7.8721	7.8925	7.8951	7.8866

Figure 13(c) and **Figure 13(d)** illustrate the hardness values of solid square parts and hollow square parts taken from the samples along the longitudinal direction, from the top layer to the bottom layer. The bar chart in the upper right corner represents the average hardness values under different scanning strategies. The three colors in the figure represent the hardness values taken from the upper, middle, and lower parts of the sample. It can be observed that the microhardness at the top of the specimen is the highest. This is due to the large temperature gradient at the top, which causes rapid grain crystallization, resulting in smaller grain sizes and higher hardness. The microhardness near the bottom is the lowest because the sedimentary layer has experienced multiple thermal cycles, leading to high heat accumulation, a small temperature difference, and a small temperature gradient. As a result, grains mainly form columnar crystals along the direction of the highest temperature gradient, and grain growth becomes coarser, reducing hardness [32]. The heterogeneity of hardness along the vertical printing direction is caused by the inherently different thermal cycles experienced at different heights during multilayer deposition [33]. This variation in thermal cycles leads to differences in grain structure and hardness across the height of the printed part. Comparing the two printing strategies, HSS and HZS, it is evident from **Figure 13(b)** and **Figure 13(d)** that the average hardness of HSS printed along the horizontal direction is 212.3 HV. In the vertical direction, the average hardness values for the top, middle, and bottom sections are 216.3 HV, 212.6 HV, and 208.6 HV,

respectively. In contrast, the average hardness of HZS printed in the horizontal direction is 201.6 HV, while the top, middle, and bottom sections in the longitudinal direction show average hardness values of 207.3 HV, 203.6 HV, and 200.4 HV, respectively. This indicates that the average hardness of samples printed using the HSS strategy is consistently higher than that of those printed with the HZS strategy, both in the transverse and longitudinal directions.

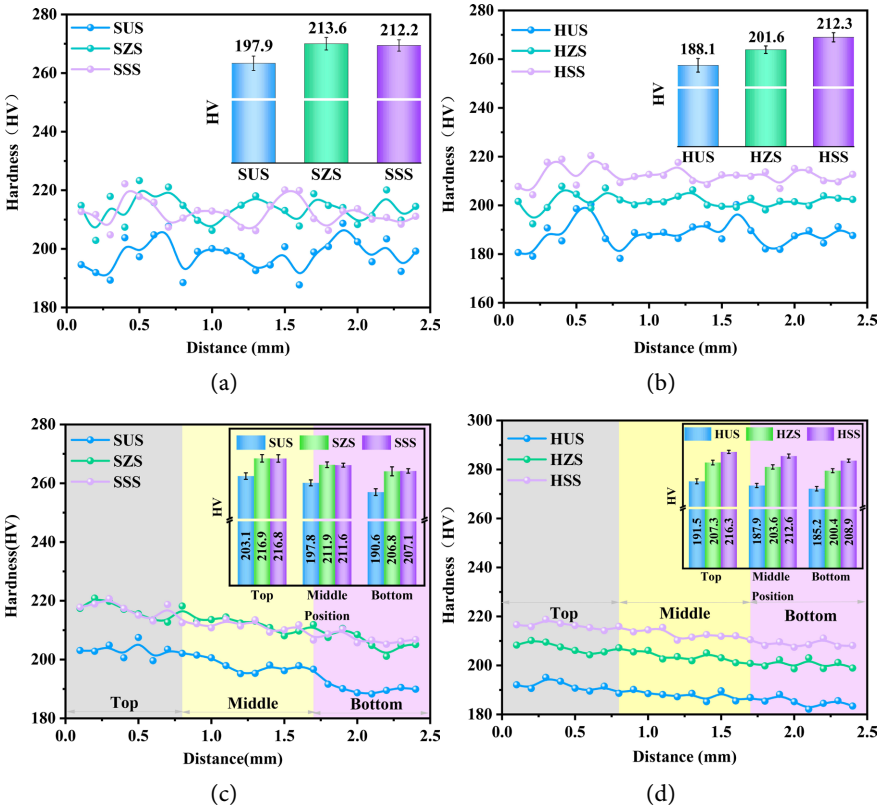

Figure 13. (a) solid square sample along the lateral hardness test curve; (b) hollow square sample along the lateral hardness test curve; (c) vertical hardness test curve of the solid square sample; (d) vertical hardness test curve of the hollow square sample.

4. Conclusion

In LDED, the scanning strategy critically impacts the quality and performance of the final part. Different scanning strategies significantly affect the microstructure, mechanical properties, and surface quality of the final molded part. This paper utilizes US, ZS, and SS deposition strategies to fabricate the solid square and the hollow square parts. Six samples were analyzed through laser scanning, XRD composition analysis, electron microscopy, density testing, and microhardness testing. A comparative analysis revealed that the US deposition strategy resulted in large interlayer melting defects and the lowest hardness for both solid and perforated parts. Due to excessive initial intermediate heat accumulation, physical parts fabricated under the SS deposition strategy exhibited significant deformation. However, compared to the US and ZS strategies, the SS scanning strategy greatly reduced

short-edge printing in experimental hollow square parts, thereby significantly improving mechanical properties. Reducing the printing for minimizing short-edges effectively improves the molding quality of printed parts.

Conflicts of Interest

The authors declare no conflicts of interest regarding the publication of this paper.

References

[1] Duan, C., Cao, X., Luo, X., Shang, D. and Hao, X. (2023) Multi-Physics Investigations on the Gas-Powder Flow and the Molten Pool Dynamics during Directed Energy Deposition Process. *Journal of Manufacturing Science and Engineering*, **145**, Article 081008. https://doi.org/10.1115/1.4062259

[2] Uriondo, A., Esperon-Miguez, M. and Perinpanayagam, S. (2015) The Present and Future of Additive Manufacturing in the Aerospace Sector: A Review of Important Aspects. Proceedings of the Institution of Mechanical Engineers, *Part G*: *Journal of Aerospace Engineering*, **229**, 2132-2147. https://doi.org/10.1177/0954410014568797

[3] Kok, Y., Tan, X.P., Wang, P., Nai, M.L.S., Loh, N.H., Liu, E., *et al.* (2018) Anisotropy and Heterogeneity of Microstructure and Mechanical Properties in Metal Additive Manufacturing: A Critical Review. *Materials & Design*, **139**, 565-586. https://doi.org/10.1016/j.matdes.2017.11.021

[4] Yuan, L., Ding, S. and Wen, C. (2019) Additive Manufacturing Technology for Porous Metal Implant Applications and Triple Minimal Surface Structures: A Review. *Bioactive Materials*, **4**, 56-70. https://doi.org/10.1016/j.bioactmat.2018.12.003

[5] Kaikai, X., Yadong, G. and Qiang, Z. (2022) Numerical Simulation of Dynamic Analysis of Molten Pool in the Process of Direct Energy Deposition. The International *Journal of Advanced Manufacturing Technology*, **124**, 2451-2461. https://doi.org/10.1007/s00170-022-10271-7

[6] Svetlizky, D., Das, M., Zheng, B., Vyatskikh, A.L., Bose, S., Bandyopadhyay, A., *et al.* (2021) Directed Energy Deposition (DED) Additive Manufacturing: Physical Characteristics, Defects, Challenges and Applications. *Materials Today*, **49**, 271-295. https://doi.org/10.1016/j.mattod.2021.03.020

[7] Mu, J., Sun, T., Leung, C.L.A., Oliveira, J.P., Wu, Y., Wang, H., *et al.* (2023) Application of Electrochemical Polishing in Surface Treatment of Additively Manufactured Structures: A Review. *Progress in Materials Science*, **136**, Article 101109. https://doi.org/10.1016/j.pmatsci.2023.101109

[8] Zhao, M., Wei, H., Mao, Y., Zhang, C., Liu, T. and Liao, W. (2023) Predictions of Additive Manufacturing Process Parameters and Molten Pool Dimensions with a Physics-Informed Deep Learning Model. *Engineering*, **23**, 181-195. https://doi.org/10.1016/j.eng.2022.09.015

[9] Rajan, V.T., Srinivasan, V. and Tarabanis, K.A. (2001) The Optimal Zigzag Direction for Filling a Two-Dimensional Region. *Rapid Prototyping Journal*, **7**, 231-241. https://doi.org/10.1108/13552540110410431

[10] Jin, G.Q., Li, W.D. and Gao, L. (2013) An Adaptive Process Planning Approach of Rapid Prototyping and Manufacturing. *Robotics and Computer-Integrated Manufacturing*, **29**, 23-38. https://doi.org/10.1016/j.rcim.2012.07.001

[11] Syed, A.K., Zhang, X., Caballero, A., Shamir, M. and Williams, S. (2021) Influence of Deposition Strategies on Tensile and Fatigue Properties in a Wire+Arc Additive Manufactured Ti-6Al-4V. *International Journal of Fatigue*, **149**, Article 106268.

https://doi.org/10.1016/j.ijfatigue.2021.106268

[12] Bi, M., Xia, L., Tran, P., Li, Z., Wan, Q., Wang, L., *et al.* (2022) Continuous Contour-Zigzag Hybrid Toolpath for Large Format Additive Manufacturing. *Additive Manufacturing*, **55**, Article 102822. https://doi.org/10.1016/j.addma.2022.102822

[13] Veiga, F., Arizmendi, M., Suarez, A., Bilbao, J. and Uralde, V. (2022) Different Path Strategies for Directed Energy Deposition of Crossing Intersections from Stainless Steel SS316L-Si. *Journal of Manufacturing Processes*, **84**, 953-964. https://doi.org/10.1016/j.jmapro.2022.10.039

[14] Tarchoun, B., Ouafi, A.E. and Chebak, A. (2020) Experimental Investigation of Laser Surface Hardening of AISI 4340 Steel Using Different Laser Scanning Patterns. *Journal of Minerals and Materials Characterization and Engineering*, **8**, 9-26. https://doi.org/10.4236/jmmce.2020.82002

[15] Tarchoun, B., El Ouafi, A. and Chebak, A. (2020) Numerical Investigation of Laser Surface Hardening of AISI 4340 Using 3D FEM Model for Thermal Analysis of Different Laser Scanning Patterns. *Modeling and Numerical Simulation of Material Science*, **10**, 31-54. https://doi.org/10.4236/mnsms.2020.103003

[16] Demin, V.N., Borisov, V.O., Grachev, G.N., Smirnov, A.L., Khomyakov, M.N. and Bagayev, S.N. (2021) Laser-Plasma Deposition of Silicon Carbonitride Films by the HMDS Vapor Gas Flow Activation after a Laser Beam Focus. *Advances in Materials Physics and Chemistry*, **11**, 121-130. https://doi.org/10.4236/ampc.2021.117012

[17] Wang, X., Wang, A. and Li, Y. (2019) A Sequential Path-Planning Methodology for Wire and Arc Additive Manufacturing Based on a Water-Pouring Rule. *The International Journal of Advanced Manufacturing Technology*, **103**, 3813-3830. https://doi.org/10.1007/s00170-019-03706-1

[18] Singh, S., Singh, A., Kapil, S. and Das, M. (2022) Utilization of a TSP Solver for Generating Non-Retractable, Direction Favouring Toolpath for Additive Manufacturing. *Additive Manufacturing*, **59**, Article 103126. https://doi.org/10.1016/j.addma.2022.103126

[19] Petrik, J. and Bambach, M. (2023) Reinforcement Learning and Optimization Based Path Planning for Thin-Walled Structures in Wire Arc Additive Manufacturing. *Journal of Manufacturing Processes*, **93**, 75-89. https://doi.org/10.1016/j.jmapro.2023.03.013

[20] Foroozmehr, E. and Kovacevic, R. (2010) Effect of Path Planning on the Laser Powder Deposition Process: Thermal and Structural Evaluation. *The International Journal of Advanced Manufacturing Technology*, **51**, 659-669. https://doi.org/10.1007/s00170-010-2659-6

[21] Sun, L., Ren, X., He, J. and Zhang, Z. (2021) Numerical Investigation of a Novel Pattern for Reducing Residual Stress in Metal Additive Manufacturing. *Journal of Materials Science & Technology*, **67**, 11-22. https://doi.org/10.1016/j.jmst.2020.05.080

[22] Ren, K., Chew, Y., Zhang, Y.F., Bi, G.J. and Fuh, J.Y.H. (2019) Thermal Analyses for Optimal Scanning Pattern Evaluation in Laser Aided Additive Manufacturing. *Journal of Materials Processing Technology*, **271**, 178-188. https://doi.org/10.1016/j.jmatprotec.2019.03.029

[23] Zhou, Z., Shen, H., Lin, J., Liu, B. and Sheng, X. (2022) Continuous Tool-Path Planning for Optimizing Thermo-Mechanical Properties in Wire-Arc Additive Manufacturing: An Evolutional Method. *Journal of Manufacturing Processes*, **83**, 354-373. https://doi.org/10.1016/j.jmapro.2022.09.009

[24] Feldhausen, T., Kannan, R., Saleeby, K., Haley, J., Kurfess, R., Bourdages, D., *et al.* (2022) Performance of Discontinuity-Free Components Produced by Additive Turning

Computer Aided Manufacturing Strategy. *Journal of Materials Processing Technology*, **308**, Article 117732. https://doi.org/10.1016/j.jmatprotec.2022.117732

[25] Jia, H., Sun, H., Wang, H., Wu, Y. and Wang, H. (2021) Scanning Strategy in Selective Laser Melting (SLM): A Review. *The International Journal of Advanced Manufacturing Technology*, **113**, 2413-2435. https://doi.org/10.1007/s00170-021-06810-3

[26] Larimian, T., Kannan, M., Grzesiak, D., AlMangour, B. and Borkar, T. (2020) Effect of Energy Density and Scanning Strategy on Densification, Microstructure and Mechanical Properties of 316L Stainless Steel Processed via Selective Laser Melting. *Materials Science and Engineering: A*, **770**, Article 138455. https://doi.org/10.1016/j.msea.2019.138455

[27] Bai, S., Perevoshchikova, N., Sha, Y. and Wu, X. (2019) The Effects of Selective Laser Melting Process Parameters on Relative Density of the Alsi10mg Parts and Suitable Procedures of the Archimedes Method. *Applied Sciences*, **9**, Article 583. https://doi.org/10.3390/app9030583

[28] Shin, W., Son, B., Song, W., Sohn, H., Jang, H., Kim, Y., *et al.* (2021) Heat Treatment Effect on the Microstructure, Mechanical Properties, and Wear Behaviors of Stainless Steel 316L Prepared via Selective Laser Melting. *Materials Science and Engineering: A*, **806**, Article 140805. https://doi.org/10.1016/j.msea.2021.140805

[29] Zhang, K., Geng, J., Liu, W., Wang, W., Wang, H., Jiang, X., *et al.* (2023) Influences of Scanning Strategy on the Quality, Accuracy, Microstructure and Performance of Inconel 625 Parts by Lam. *Journal of Materials Research and Technology*, **26**, 1962-1983. https://doi.org/10.1016/j.jmrt.2023.08.024

[30] Smoqi, Z. (2022) M3AM: Materials, Monitoring, and Machine Learning for Flaw-Free Additive Manufacturing. Dissertation, The University of Nebraska-Lincoln.

[31] Kistler, N.A., Corbin, D.J., Nassar, A.R., Reutzel, E.W. and Beese, A.M. (2019) Effect of Processing Conditions on the Microstructure, Porosity, and Mechanical Properties of Ti-6Al-4V Repair Fabricated by Directed Energy Deposition. *Journal of Materials Processing Technology*, **264**, 172-181. https://doi.org/10.1016/j.jmatprotec.2018.08.041

[32] Sun, G., Sun, X., Zhao, X. and Chen, C. (2024) Effect of Interlayer Rapid Cooling on the Microstructure and Properties of Aluminum Alloys Produced by Wire Arc Additive Manufacturing. *Manufacturing Letters*, **40**, 70-74. https://doi.org/10.1016/j.mfglet.2024.03.001

[33] Wang, T., Kang, J., Darnell, M. and Liu, X. (2023) Ultrasonically Assisted Hot-Wire Arc Additive Manufacturing Process of AA7075 Metal Matrix Nanocomposite. *Journal of Alloys and Compounds*, **936**, Article 168298. https://doi.org/10.1016/j.jallcom.2022.168298